Copyright 2003 by the Society of Photo-Optical Instrumentation Engineers.

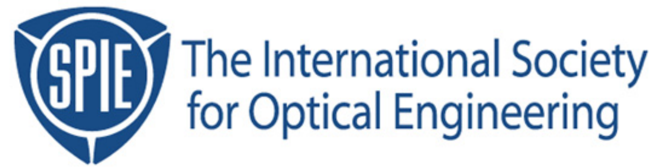

This paper was published in the proceedings of
Optical Microlithography XVI, SPIE Vol. 5040, pp. 57-68.
It is made available as an electronic reprint with permission of SPIE.

One print or electronic copy may be made for personal use only. Systematic or multiple reproduction, distribution to multiple locations via electronic or other means, duplication of any material in this paper for a fee or for commercial purposes, or modification of the content of the paper are prohibited.

Methods for Benchmarking Photolithography Simulators

Mark D. Smith*, Chris A. Mack
KLA-Tencor Corp.

ABSTRACT
Numerical simulation has become an indispensable tool for the design and optimization of photolithographic processes. Because the semiconductor industry now relies heavily on these tools, it is necessary to be able to benchmark their accuracy – as feature sizes continue to shrink, the numerical error in these simulators must decrease as well [1]. Fortunately, there is a large body of literature from the optics community that can be used to benchmark the absolute accuracy of an aerial image calculation. We present a suite of closed-form solutions that are particularly relevant to optical lithography simulation. Our tests include solutions for both scalar and vector imaging models and for imaging with and without aberrations. These tests will be used to demonstrate how to identify many of the common numerical problems that can arise when performing aerial image calculations, and the closed-form solutions will be outlined in a form that will allow the tests to be applied to any aerial image simulator. Specific results will be presented for PROLITH and SPLAT. Both of these simulators give results that are in agreement with the closed-form test problems.

Keywords: Lithography simulation, numerical accuracy, PROLITH, SPLAT

1 INTRODUCTION

As numerical simulation becomes more important to the design and optimization of photolithographic processes, it becomes vital that simulators provide accurate results. Benchmarking the accuracy of a simulator should be an important part of an "acceptance test" for all simulation software. This is true if you have purchased a commercial simulator (such as PROLITH) or if you are using a code that you or your colleagues have written for internal use at your company. Although it is obvious that software must be free of bugs or algorithm problems in order to make quantitative engineering decisions, few users of simulation software actually perform a quantitative study of the accuracy of their simulator.

One of the reasons relatively few quantitative accuracy studies are performed is that for the end-user of a simulator, it is often difficult to make a judgment regarding the accuracy of a simulator beyond whether a particular result is "reasonable". Of course, it is possible to compare one simulator with the results calculated with another simulator, but if the results do not agree, how do you decide which one is correct? In addition, both simulators could agree and still be incorrect. The approach taken in the current study is to find closed-form solutions from the research literature, and to use these solutions as an absolute standard for benchmarking lithography simulators. This is similar to the approach taken by Brunner [2] and Gordon [3]. We concentrate in this work on aerial image calculations because there is a vast optic literature, the physics is well understood, and the accuracy of the following simulation steps, such as expose, PEB or develop, depends on the accuracy of the results from optics calculations.

The benchmarks presented here have been chosen to be especially relevant to optical lithography. All of the tests outlined here are in the Fraunhofer diffraction limit and use partially coherent source shapes. Tests are described for imaging with and without aberrations, for both scalar and vector imaging models. In addition, the metrics that are used to determine the accuracy of the results are also directly relevant to lithography – we report errors in image CD and image placement. The outline of this paper is as follows: In Section 2, we present the Abbe formulation of the imaging problem, and in Section 3, we draw attention to the aspects of the imaging problem that give rise to numerical difficulties. The first test is presented in Section 4. This test describes imaging of a dense line-space pattern with a perfect lens, using a scalar imaging model. Imaging tests that include lens aberrations are presented in Section 5, where we perform calculations with both scalar and vector imaging models.

* mark.d.smith@kla-tencor.com; phone 1-512-381-2318; 8834 North Capital of Texas Highway, Suite 301, Austin, TX 78759

2 THE ABBE FORMULATION OF THE IMAGING PROBLEM

We will model partially coherent source shapes by using the Abbe formulation of the imaging problem, where the source shape is constructed as an incoherent sum of source points. Mathematically, the Abbe formulation (in one dimension for simplicity) is given by

$$I(x) = \frac{\iint \vec{E}(x,S_x,S_y) \bullet \vec{E}^*(x,S_x,S_y) S(S_x,S_y) dS_x dS_y}{I_N} \tag{1}$$

where $I(x)$ is the "intensity" (irradiance), the function $S(S_x,S_y)$ describes the shape and intensity of the source, $\vec{E}(x,S_x,S_y)$ gives the electric field at the wafer due to a source point located at (S_x,S_y), and the term I_N is the normalization of the aerial image intensity. This is chosen to give unit intensity at the mask, so

$$I_N = \iint S(S_x,S_y) dS_x dS_y \tag{2}$$

If $\lambda/(NA \cdot p) < 1 < 2\lambda/(NA \cdot p)$, then the electric field is described by a three-term Fourier series

$$\begin{aligned} \vec{E}(x,S_x,S_y) = f_{-1}\vec{P}\left(-\frac{\lambda}{NA \cdot p} - S_x, -S_y\right)\exp\left[-\frac{2\pi i x}{p}\right] + f_0\vec{P}\left(-S_x,-S_y\right) \\ + f_{+1}\vec{P}\left(\frac{\lambda}{NA \cdot p} - S_x, -S_y\right)\exp\left[\frac{2\pi i x}{p}\right] \end{aligned} \tag{3}$$

where p is the pitch of the line-space pattern (wafer-scale), and the symbols f_n are the Fourier coefficients. For a binary line-space pattern on the mask, the Fourier coefficients are given by

$$\begin{aligned} f_{\pm 1} &= -\frac{1}{\pi}\sin\left(\frac{\pi w}{p}\right) \\ f_0 &= \frac{p-w}{p} \end{aligned} \tag{4}$$

where $x = 0$ is the center of a line of width w. The pupil function $\vec{P}(r,\theta)$ includes aberrations, the radiometric correction, and the correspondence between pupil position and the vector components of the electric field at the wafer. The pupil function can be written in plane-polar coordinates, where the radial coordinate is normalized to be one at the outer edge of the lens. This leads to

$$\vec{P}(r,\theta) = Circ(r)\exp(2\pi i W(r,\theta))\left(\frac{1-\frac{NA^2 r^2}{R^2}}{1-NA^2 r^2}\right)^{1/4} \vec{e}(r,\theta) \tag{5}$$

where the $Circ(r)$ function filters out the diffraction orders that do not pass through the lens, the second term describes the influence of aberrations through the a series of Zernike polynomials $W(r,\theta)$, the third term is the radiometric

correction[4,5,6] with a reduction ratio of R, and the final term $\vec{e}(r,\theta)$ describes the dependence of the electric field vector components on the position in the pupil. This function can be derived by considering the effect of a spherical lens on x-polarized and y-polarized light [7,8]. For x-polarized light, the x-, y-, and z-components of the electric field components at the wafer become:

$$\vec{e}(r,\theta)=\begin{bmatrix}\sqrt{1-(NA\cdot r)^2}\cos^2\theta+\sin^2\theta\\ \frac{1}{2}\left(\sqrt{1-(NA\cdot r)^2}-1\right)\sin 2\theta\\ -NA\cdot r\cos\theta\end{bmatrix} \tag{6}$$

For y-polarized light, the x-, y-, and z-components of the electric field components at the wafer become

$$\vec{e}(r,\theta)=\begin{bmatrix}\frac{1}{2}\left(\sqrt{1-(NA\cdot r)^2}-1\right)\sin 2\theta\\ \sqrt{1-(NA\cdot r)^2}\sin^2\theta+\frac{1}{2}(1+\cos 2\theta)\\ -NA\cdot r\sin\theta\end{bmatrix} \tag{7}$$

The intensity for unpolarized light can be found by taking an average of the intensities from x-polarized and y-polarized illumination. If we wish to examine a scalar imaging model, then we can use Equation (6) in the limit as NA approaches zero:

$$\vec{e}(r,\theta)=\begin{bmatrix}1\\0\\0\end{bmatrix} \tag{8}$$

In Equations (5) to (8), the pupil function has been described in terms of polar coordinates, while in Equation (3), the pupil function is described in terms of Cartesian coordinates, as $P(f_x,f_y)$. The two representations are related by the coordinate transformation

$$\begin{aligned} f_x &= r\cos\theta \\ f_y &= r\sin\theta \end{aligned} \tag{9}$$

Finally, it is convenient to introduce the transmission cross-coefficients by writing the intensity as a Fourier-type series of the following form [9]:

$$I(x)=\sum_{n=-1}^{1}\sum_{m=-1}^{1} f_n f_m^{\,*}\, t(n,m)\exp\left[-\frac{i2\pi(n-m)x}{p}\right] \tag{10}$$

where $t(n,m)$ gives the transmission cross-coefficients, and can be calculated from Equation (1) as [9]:

$$t(n,m)=\frac{\iint \vec{P}\left(\frac{n\lambda}{NA\cdot p}-S_x,-S_y\right)\cdot \vec{P}^*\left(\frac{m\lambda}{NA\cdot p}-S_x,-S_y\right)S(S_x,S_y)dS_x dS_y}{I_N} \tag{11}$$

3 NUMERICAL INTEGRATION OF THE IMAGING EQUATIONS

The imaging equations lead to difficulties in most simulators for two reasons. First, the equations described above are nonlinear, and in general must be integrated numerically. Second, the pupil function is discontinuous at the edge of the lens and most idealized source shapes are also discontinuous functions (e.g., a top-hat function for partially coherent sources). High-accuracy numerical integration routines often assume that both the integrand and the derivatives of the integrand are continuous – this assumption is clearly violated by functions that are discontinuous. Novel approaches are required to accurately integrate the imaging equations.

The numerical integrations required to evaluate the imaging equations are generally performed by placing either a grid on the objective lens or a grid on the source shape or both. This grid is then used to numerically approximate the integral in Equation (1). In PROLITH, a grid is placed on the source, and then a partially coherent source can be approximated as the incoherent sum of coherent sources. A similar approach is taken in SPLAT [10]. Instead of using the Abbe formulation given by Equation (1), the Hopkins formulation is used in SPLAT. For the Hopkins formulation, an integration is also required, and similar numerical difficulties arise. SPLAT has two methods for performing the necessary integrals: applying a grid to the source and an adaptive integration algorithm. The source grid method is more similar to the operation of PROLITH, so the comparisons presented here will emphasize SPLAT with a source grid. The adaptive integration algorithm essentially performs the integration once, then subdivides the grid in half and performs the integration again. If the results from the first integration agree with the second integration (within an error tolerance), the programs stops and reports the results. If the results do not agree, then the integration grid is subdivided again and again until the error tolerance between two successive grids is satisfied.

In the following sections, we present test problems that highlight the numerical difficulties that arise for both the Abbe and the Hopkins formulation of the imaging equations. First, in Section 4, we examine scalar imaging with a perfect lens where the diffraction orders are "clipped" by the edge of the objective lens. This test will determine how well the numerical method handles discontinuities in the pupil function and the discontinuity in an idealized partially coherent source shape. Next, in Section 5, we examine partially coherent imaging for both scalar and vector models with lens aberrations. We will examine two cases for this test: one case where diffraction pattern is not "clipped" by the objective lens, and then a second case where the diffraction pattern is "clipped" by the objective lens. Thus, the benchmark problems presented highlight both the non-linearity due to aberrations and vector imaging and the discontinuities due to the abrupt cut-off of the source shape and the objective lens.

4 SCALAR IMAGING MODEL WITH A PARTIALLY COHERENT SOURCE AND A PERFECT LENS

As outlined in the previous section, integration of the imaging equations can be numerically difficult because the pupil function is discontinuous at the edge of the lens and most source shapes are also discontinuous functions. In this benchmark problem, the pupil "clips" the diffraction orders, so an accurate numerical method must correctly approximate the intersection between the two pupil functions and the source function in the integrand. The intersection between these different regions is shown in Figure 1 for a dense line-space pattern with a partially coherent source shape. As shown in the figure, the middle section (region II) of the source contributes normal three-beam imaging at the wafer, but there are regions along the left and right edge of the source that only contribute to the aerial image through two-beam imaging

The approach that we will take in order to derive closed-form solutions is to split the source into regions that contribute 2 and 3 beam imaging. This approach was used by Kintner [11] (and others [3,9]) to derive a solution to Equation (1) for scalar imaging with a perfect lens and no reduction (R = 1). If we split the source into the three regions, then Equation (11) becomes

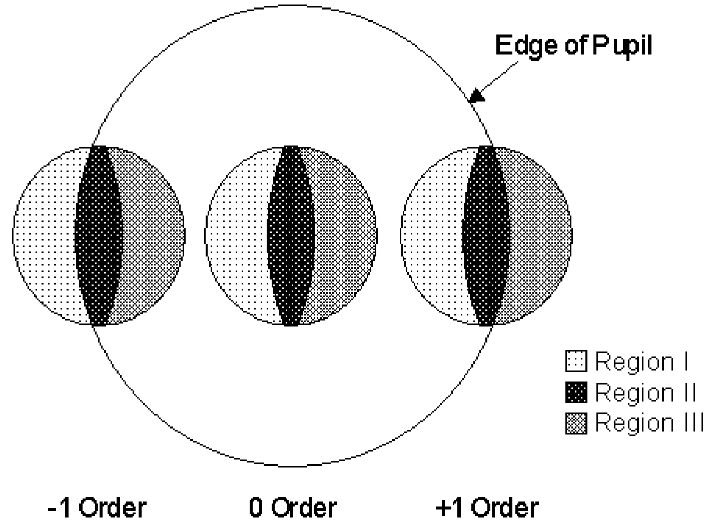

Figure 1: Schematic diagram of the –1, 0, and +1 diffraction orders from a line-space pattern combined with a partially coherent source shape. Region I is the portion of the source that contributes two-beam imaging through the 0 and +1 diffraction orders. Region II represents the portion of the source that contributes three-beam imaging, and Region III represents the portion of the source that contributes two-beam imaging through the –1 and 0 diffraction orders.

$$t(n,m)=\frac{1}{I_N}\left(\iint_{Region\ I} P\left(\frac{n\lambda}{NA\cdot p}-S_x,-S_y\right)P^*\left(\frac{m\lambda}{NA\cdot p}-S_x,-S_y\right)S(S_x,S_y)dS_x dS_y + \iint_{Region\ II} P\left(\frac{n\lambda}{NA\cdot p}-S_x,-S_y\right)P^*\left(\frac{m\lambda}{NA\cdot p}-S_x,-S_y\right)S(S_x,S_y)dS_x dS_y + \iint_{Region\ III} P\left(\frac{n\lambda}{NA\cdot p}-S_x,-S_y\right)P^*\left(\frac{m\lambda}{NA\cdot p}-S_x,-S_y\right)S(S_x,S_y)dS_x dS_y\right) \quad (12)$$

For the assumptions of a perfect lens, the pupil function is reduced to a circle function, and the integrand for each of the three integrals in Equation (12) is equal to either zero or unity. This means that each of the TCCs can be expressed in terms of the areas of the three regions. The TCCs have been evaluated and are listed in Table 1.

We now determine the areas of the three regions shown in Figure 1. The area of the Region II is given by

$$Area_{II} = 2\arccos(X_I) - 2X_I\sqrt{1-X_I^{\,2}} + 2(X_I - X_c)\sqrt{\sigma^2-(X_I-X_c)^2} + 2\sigma^2\arctan\left[\frac{X_I - X_c}{\sqrt{\sigma^2-(X_I-X_c)^2}}\right] \quad (13)$$

where X_C is the x-coordinate in the pupil plane at the center of the +1 diffraction order,

$$X_C = \frac{\lambda}{p\cdot NA}$$

and X_I is the x-coordinate in the pupil plane where the source shape intersects the pupil,

Index *n*	Index *m*	Transmission Cross-Coefficient, *t*(*n*,*m*)
-1	-1	$(Area_{II}+ Area_{III})/ \sigma^2\pi$
-1	0	$(Area_{II}+ Area_{III})/ \sigma^2\pi$
-1	1	$Area_{II}/ \sigma^2\pi$
0	-1	$(Area_{II}+ Area_{III})/ \sigma^2\pi$
0	0	1
0	1	$(Area_{I}+ Area_{II})/ \sigma^2\pi$
1	-1	$Area_{II}/ \sigma^2\pi$
1	0	$(Area_{I}+ Area_{II})/ \sigma^2\pi$
1	1	$(Area_{I}+ Area_{II})/ \sigma^2\pi$

Table 1: Transmission cross-coefficients for a dense line-space pattern with an ideal pupil function and a partially coherent source shape.

$$X_I = \frac{1 + X_C^2 - \sigma^2}{2X_C}$$

The area of the regions I and III can then be calculated from the area of region II:

$$Area_I = Area_{III} = \frac{\pi\sigma^2 - Area_{II}}{2} \tag{14}$$

In the above set of equations, it has been assumed that $X_c^2 + \sigma^2 < 1$.

By taking advantage of the fact that $Area_I = Area_{III}$, and $f_{-1} = f_{+1}$, the transmission cross-coefficients given in the table can be used to derive the final aerial image intensity at the wafer for this test problem:

$$I(x) = f_0^2 + 2\frac{Area_I + Area_{II}}{\pi\sigma^2} f_1^2 + 4\frac{Area_I + Area_{II}}{\pi\sigma^2} f_0 f_1 \cos\left(\frac{2\pi x}{p}\right) + 2\frac{Area_{II}}{\pi\sigma^2} f_1^2 \cos\left(\frac{4\pi x}{p}\right) \tag{15}$$

In order to compare with a specific result, we will choose $\lambda = 193.306$ nm, NA = 0.85, a partial coherence of 0.2, and a 120nm line pattern on a 240nm pitch. For this benchmark problem, we will calculate numerical errors in the image CD. To do this, we first calculate the intensity threshold at the mask edge by using equation (15),

$$I\left(\frac{p}{4}\right) = f_0^2 + 2\frac{Area_I}{\pi\sigma^2} f_1^2 \tag{16}$$

This intensity is approximately equal to 0.3219. Next, the image CD is calculated with PROLITH and SPLAT with the aerial image threshold value of 0.3219. The difference between the simulated result and a CD of 120nm is the error in the calculation. As shown in Figure 2, the error in the calculation generally decreases as the number of grid points is increased. For both simulators, the error is less than 1% for the finest grid spacing. For PROLITH, the error is less than 1.5% for all grid spacings.

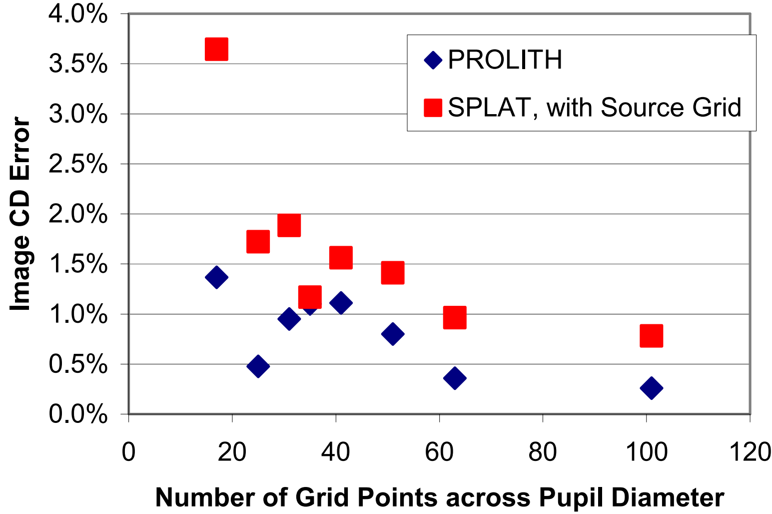

Figure 2: Error in the intensity in the image CD calculated with PROLITH and SPLAT, when SPLAT is operated with a source grid for integration of the imaging equations. When the adaptive integration method is used, SPLAT gives an error less than 0.02% of the image CD.

5 SCALAR AND VECTOR IMAGING MODELS WITH A PARTIALLY COHERENT SOURCE AND LENS ABERRATIONS

As in the previous section, we will evaluate the integrals in source coordinates over the domains where the pupil functions intersect the source function. This allows us to use the same approach as outlined by Steel [12]: because the pupil function is a smoothly varying function of f_x and f_y over these domains, we can safely expand the pupil function in a Taylor series. The integrals required to evaluate the transmission cross-coefficients are now tractable, and greater accuracy can be achieved by simply including more terms in the Taylor series. For the results presented here, all Taylor series expansions retained 6 terms.

First, we write the Taylor series expansion for the pupil function:

$$P\left(\frac{n\lambda}{NA \cdot p} - S_x, -S_y\right) = P_n + \frac{\partial P_n}{\partial f_x}\left(-S_x\right) + \frac{\partial P_n}{\partial f_y}\left(-S_y\right) + \ldots \tag{17}$$

Here, we have introduced a subscript to denote the pupil position where the pupil functions (and derivatives) are evaluated:

$$P_n \equiv P\left(\frac{n\lambda}{NA \cdot p}\right)$$

Thus, the Taylor series is an expansion about the pupil position of the diffraction orders for a coherent source, and the "small parameter" in the series expansion is the size of the partially coherent source.

Combining Equations (11) and (17) leads to:

$$t(n,m)=\frac{1}{I_N}\iint_{Source}\left[P_n-\frac{\partial P_n}{\partial f_x}S_x-\frac{\partial P_n}{\partial f_y}S_y+....\right]\cdot\left[P_m-\frac{\partial P_m}{\partial f_x}S_x-\frac{\partial P_m}{\partial f_y}S_y+....\right]^* S(S_x,S_y)dS_x dS_y$$

The integrand can now be written as a power series in the source coordinates S_x and S_y:

$$\sum_{j=0}^{\infty}\sum_{k=0}^{\infty}C_{jk}(n,m)S_x{}^jS_y{}^k = \left[P_n-\frac{\partial P_n}{\partial f_x}S_x-\frac{\partial P_n}{\partial f_y}S_y+....\right]\cdot\left[P_m-\frac{\partial P_m}{\partial f_x}S_x-\frac{\partial P_m}{\partial f_y}S_y+....\right]^* \quad (18)$$

where coefficients $C_{jk}(n,m)$ through quadratic terms in S_x and S_y are given by

$$\begin{aligned}
C_{00}(n,m)&=P_nP_m{}^*\\
C_{10}(n,m)&=-P_n\frac{\partial P_m{}^*}{\partial f_x}-\frac{\partial P_n}{\partial f_x}P_m{}^*\\
C_{01}(n,m)&=-P_n\frac{\partial P_m{}^*}{\partial f_y}-\frac{\partial P_n}{\partial f_y}P_m{}^*\\
C_{11}(n,m)&=P_n\frac{\partial^2 P_m{}^*}{\partial f_x\partial f_y}+\frac{\partial^2 P_n}{\partial f_x\partial f_y}P_m{}^*+\frac{\partial P_n}{\partial f_x}\frac{\partial P_m{}^*}{\partial f_y}+\frac{\partial P_n}{\partial f_y}\frac{\partial P_m{}^*}{\partial f_x}\\
C_{20}(n,m)&=\frac{1}{2}P_n\frac{\partial^2 P_m{}^*}{\partial f_x{}^2}+\frac{\partial P_n}{\partial f_x}\frac{\partial P_m{}^*}{\partial f_x}+\frac{1}{2}\frac{\partial^2 P_n}{\partial f_x{}^2}P_m{}^*\\
C_{02}(n,m)&=\frac{1}{2}P_n\frac{\partial^2 P_m{}^*}{\partial f_y{}^2}+\frac{\partial P_n}{\partial f_y}\frac{\partial P_m{}^*}{\partial f_y}+\frac{1}{2}\frac{\partial^2 P_n}{\partial f_y{}^2}P_m{}^*
\end{aligned} \quad (19)$$

5.1 Special Case: No "Clipping" by the Pupil

For a dense line-space pattern, where the pupil does not "clip" the +1 and –1 diffraction orders (i.e., $\lambda/(NA\cdot p)+\sigma<1$), then each source point contributes to three beam imaging. This leads to the final equation for the transmission cross-coefficients

$$t(n,m)=\sum_{j=0}^{\infty}\sum_{k=0}^{\infty}C_{jk}(n,m)\iint_{Source}S_x{}^jS_y{}^k dS_x dS_y \quad (20)$$

The integrals in the above equation can be evaluated in terms of the gamma function:

$$\int_{-\sigma}^{\sigma}\left(\int_{-\sqrt{\sigma^2-S_x{}^2}}^{\sqrt{\sigma^2-S_x{}^2}}S_x{}^jS_y{}^k dS_y\right)dS_x=\frac{\left[1+(-1)^j\right]\left[1+(-1)^k\right]}{4}\frac{\sigma^{2+j+k}\Gamma\left(\frac{j+1}{2}\right)\Gamma\left(\frac{k+1}{2}\right)}{4\Gamma\left(\frac{j+k+4}{2}\right)} \quad (21)$$

For this test problem, we will use a scalar imaging model with NA = 0.85, λ = 193.306 nm, and σ = 0.2 for a binary mask with 150 nm lines on a 300 nm pitch. The aberration is 0.1 waves of coma (maximum OPD), which corresponds to the pupil function given by

$$P(r,\theta) = Circ(r) \cdot \exp\{i2\pi \cdot 0.1(3r^2 - 2)r\cos\theta\} \tag{22}$$

From the closed-form solution, we can also calculate the image placement position. We use the following procedure to do this. First, we calculate an aerial image without aberrations, and determine the intensity value at the feature edge. This intensity value is 0.25. Next, we locate the edge positions of the left and right sides of the feature for the aberrated image by using the previously determined aerial image intensity threshold value (0.25). The image placement position is the average of the positions of the left and right edges. For the closed-form solution, we find the image placement position to be 3.648 nm. This value can be used to construct a graph of the error versus the number of grid points, as shown in Figure 3. As shown in the figure, the errors are quite small – in most cases, the numerical error in the image placement is smaller than the diameter of a carbon atom!

We can also repeat this test with the vector imaging model in PROLITH. (SPLAT currently only performs scalar imaging calculations.) For this case, the different components of the electric field vector will depend on pupil position, see Equations (6) and (7). This can easily be accommodated with the current approach by including these terms in the pupil functions, and then again expanding in a Taylor series. One aerial image will be calculated for each vector component of the electric field for each polarization – this gives a total of six aerial images that are averaged to give the final result. It should be noted that Equations (6) and (7) contain the square-root function, and a Taylor series is not guaranteed to converge for any argument of the square root function. However, this problem arises only when the argument of the square root is equal to zero [13], which can only occur in Equations (6) and (7) when $NA \geq 1$. Because we are not interested in this case, the solutions presented here should be well-behaved and converge to the exact solution for the imaging equations.

The image placement position for the vector imaging model with coma is found following the same procedure as outlined above for the scalar imaging results. The intensity at the feature edge without aberrations is approximately equal to 0.3356, and when this threshold value is used to determine the left and right feature edges in the aberrated image, the placement position is found to be 3.814 nm. Numerical errors calculated using the vector, unpolarized imaging model in PROLITH are shown in Figure 4. As shown in the figure, the errors are quite small for all of the source grid spacings investigated in this study.

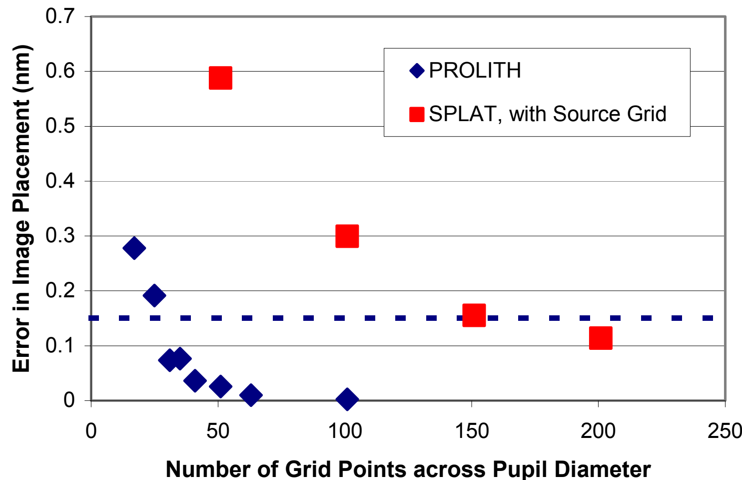

Figure 3: Numerical error in the image placement position as calculated with PROLITH and SPLAT (with a source grid) as a function of the number of source grid points. The error for SPLAT with adaptive integration was less than 0.02%. For comparison, the dashed line shows the diameter of a carbon atom. The test case is for a pattern of 150nm lines on a 300 nm pitch for λ = 193.306, NA = 0.85, and σ = 0.2 with 0.1 waves of coma (maximum OPD).

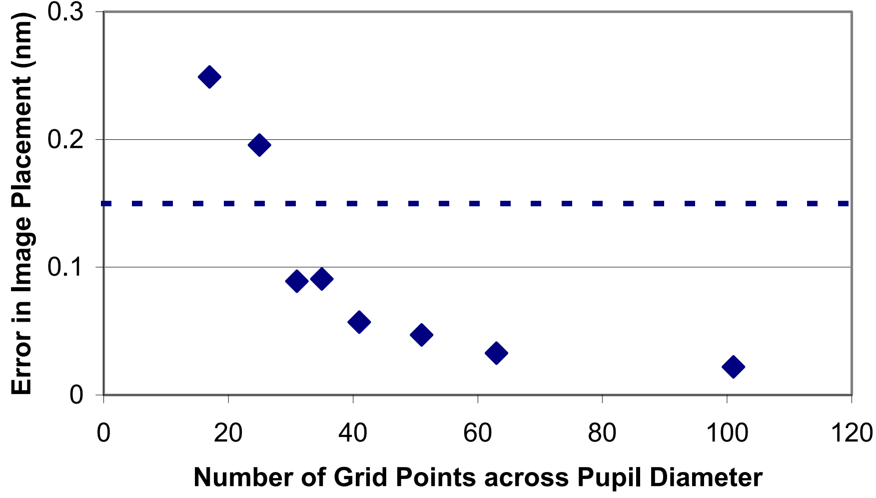

Figure 4: Numerical error in the image placement error as calculated with the vector, unpolarized model in PROLITH. For comparison, the dashed line shows the diameter of a carbon atom. The test case is for a pattern of 150nm lines on a 300 nm pitch for $\lambda = 193.306$, NA = 0.85, and $\sigma = 0.2$ with 0.1 waves of coma (maximum OPD).

5.2 General Case: Imaging with "Clipping" by the Pupil

When the source region intersects the pupil regions as shown in Figure 1, then the integrals for the transmission cross-coefficients must be performed over the same domains as used to evaluate the Kintner results in the Section 4. The following identity will be required to evaluate the necessary integrals:

$$\int_{x_1}^{x_2}\left(\int_{-\sqrt{\sigma^2-x^2}}^{\sqrt{\sigma^2-x^2}} x^j y^k dy\right)dx = \frac{\left[1+(-1)^k\right]}{2}\frac{\sigma^{j+k+2}}{(k+1)}\left[Sign[x_2]^{j+1} B_{\left(\frac{x_2}{\sigma}\right)^2}\left(\frac{j+1}{2},\frac{k+3}{2}\right) - Sign[x_1]^{j+1} B_{\left(\frac{x_1}{\sigma}\right)^2}\left(\frac{j+1}{2},\frac{k+3}{2}\right)\right] \quad (23)$$

Note that the integral in the above equation is performed over source coordinates (S_x,S_y), but the coordinates (x,y) have been substituted in order to simplify the notation. The function $B_z(a,b)$ is the incomplete beta function:

$$B_z(a,b) = \int_0^z t^{a-1}(1-t)^{b-1} dt$$

For the region II shown in Figure 1, we obtain the following result:

$$\iint\limits_{Region\ II} (S_x)^j (S_y)^k \, dS_y dS_x = \int\limits_{-(X_I - X_c)}^{X_I - X_c} \left(\int\limits_{-\sqrt{\sigma^2 - S_x^{\,2}}}^{\sqrt{\sigma^2 - S_x^{\,2}}} (S_x)^j (S_y)^k \, dS_y \right) dS_x + \int\limits_{X_I - X_C}^{1 - X_c} \left(\int\limits_{-\sqrt{1-(S_x + X_c)^2}}^{\sqrt{1-(S_x + X_c)^2}} (S_x)^j (S_y)^k \, dS_y \right) dS_x$$

$$+ \int\limits_{-(1-X_C)}^{-(X_I - X_C)} \left(\int\limits_{-\sqrt{1-(X_c - S_x)^2}}^{\sqrt{1-(X_c - S_x)^2}} (S_x)^j (S_y)^k \, dS_y \right) dS_x$$

The last two integrals in the above equation can be put into the form of Equation (23) by a change of variable. We demonstrate this for the second integral, where we choose $\eta = S_x + X_c$:

$$\int\limits_{X_I - X_C}^{1 - X_C} \left(\int\limits_{-\sqrt{1-(S_x - X_C)^2}}^{\sqrt{1-(S_x - X_C)^2}} (S_x)^j (S_y)^k \, dS_y \right) dS_x = \int\limits_{X_I}^{1} \left(\int\limits_{-\sqrt{1-\eta^2}}^{\sqrt{1-\eta^2}} (\eta - X_C)^j (S_y)^k \, dS_y \right) d\eta$$

$$= \sum_{m=0}^{j} \binom{j}{m} (-X_C)^m \int\limits_{X_I}^{1} \left(\int\limits_{-\sqrt{1-\eta^2}}^{\sqrt{1-\eta^2}} \eta^{j-m} (S_y)^k \, dS_y \right) d\eta \qquad (24)$$

where the binomial coefficients are given by

$$\binom{j}{m} = \frac{j!}{(j-m)!\,m!}$$

Similar results can be derived for regions I and III.

For this test problem, we will examine results for a vector imaging model with a reduction factor of $R = 4$, NA = 0.85, λ = 193.306 nm, and $\sigma = 0.2$ for a binary mask with 120 nm lines on a 240 nm pitch. The aberration is 0.1 waves of coma (maximum OPD), which corresponds to the pupil function given by Equation (22).

From the closed-form solution, we can also calculate the image placement error as described in Section 5.1. First, we calculate the aerial image threshold without aberrations at the feature edge – this value is approximately 0.4190. From this we find the image placement error for the case with coma to be –6.730 nm. This value can be used to construct a graph of the error versus the number of grid points, as shown in Figure 5.

6 SUMMARY AND CONCLUSIONS

In this study we have presented benchmark problems for aerial image simulators. In the first benchmark problem, the diffraction pattern is "clipped" by the edge of an ideal objective lens. This leads to a discontinuity in the integrand in the Abbe formulation of the imaging problem. Both PROLITH and SPLAT converged to the correct aerial image CD as predicted by the closed-form solution by Kintner [11], and this indicates that these simulators are both accurate and robust in spite of the numerical problems that may be caused by "clipping" by the edge of the pupil. Accurate calculations for a non-ideal lens were presented in the second benchmark problem, where the pupil function includes the nonlinear terms due to aberrations and the vector nature of light. Again, both PROLITH and SPLAT demonstrated good results, converging to the closed-form solution by Steel [12]. In the last benchmark problem, the vector imaging model in PROLITH demonstrated good agreement when both vector imaging, lens aberrations, the radiometric correction, and "clipping" were included in the imaging model.

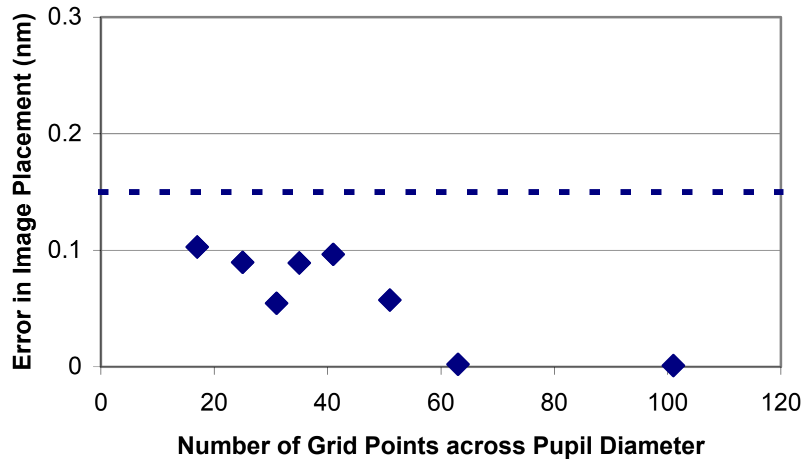

Figure 5: Numerical error in the image placement as calculated with the vector, unpolarized model in PROLITH. The dashed line shows the diameter of a carbon atom. The test case is for a pattern of 120nm lines on a 240 nm pitch for a reduction factor of R = 4, λ = 193.306, NA = 0.85, and σ = 0.2 with 0.1 waves of coma (maximum OPD).

This study demonstrates the importance of benchmarking simulators against known, closed-form solutions. Because the optics literature is so vast, there must be many other interesting benchmark problems that could be used to test the accuracy of optical lithography simulators. One of the main goals of our benchmarking efforts is to collect useful tests that can be used by the lithography community to establish the accuracy of lithography simulators. At this point we can only encourage other researchers to highlight solutions that we have missed in their own benchmarking efforts, and to continue to derive new results that can be used to improve the accuracy of simulators in the future.

7 REFERENCES

1. ITRS Roadmap, 2000 Update.
2. T. Brunner, “SEMATECH Report: Benchmark tests for image simulation programs used in optical lithography”, SEMATECH (1994).
3. R.L. Gordon, “Exact Computation of 2D Aerial Imagry,” *Proc. SPIE*, Vol. 4692 (2002) pp. 517-528.
4. C.A. Mack, *Inside PROLITH: A Comprehensive Guide to Optical Lithography Simulation*, FINLE Technologies (Austin, TX: 1997).
5. D.C. Cole, E. Barouch, U. Hollerbach, and S.A. Orzag, “Extending Scalar Aerial Image Calculations to Higher Numerical Apertures,” *Journal of Vacuum Science and Technology*, Vol. B10, No. 6 (Nov/Dec, 1992) pp. 3037-3041.
6. M. Born and E. Wolf, *Principles of Optics*, 6th edition, Pergamon Press (Oxford, 1980) pp. 113-117.
7. M. Mansuripur, “Distribution of light at and near the focus of high-numerical-aperture objectives,” *Journal of the Optical Society of America Part A,* Vol. 3 (1986) pp 2086-2093.
8. D.G. Flagello, T. Milster, A.E. Rosenbluth, “Theory of high-NA imaging in homogeneous thin films,” *Journal of the Optical Society of America Part A,* Vol. 13 (1996) pp 53-64.
9. H.H. Hopkins, “On the diffraction theory of optical images,” *Proc. Royal Soc. A*, Vol. 217 (1953) pp. 408-432
10. SPLAT was written by the D. Lee, D. Newmark, K. Toh, P. Flanner, and A.R. Neurether in the SAMPLE Group in the Electrical Engineering and Computer Science Department of the University of California, Berkeley.
11. E.C. Kintner, “Method for the calculation of partially coherent imagery,” *Applied Optics*, Vol. 17 (Sept, 1978) pp. 2747-2753.
12. W.H. Steel, “Effects of Small Aberrations on the Images of Partially Coherent Objects,” *Journal of the Optical Society of America,* Vol. 47 (1957) pp 405-413.
13. M. Abramowitz and I.A. Stegun, *Handbook of Mathematical Functions*, Dover (New York, NY: 1965)